ceramics

MDPI

Article

Structure and Relaxor Behavior of (0.5 − x)$BiFeO_3$-0.5$PbFe_{0.5}Nb_{0.5}O_3$-$xPbTiO_3$ Ternary Ceramics

Nikita A. Boldyrev [1,*], Eugene I. Sitalo [1], Lidia A. Shilkina [1], Alexander V. Nazarenko [2], Andrei D. Ushakov [3], Vladimir Y. Shur [3], Larisa A. Reznichenko [1] and Ekaterina V. Glazunova [1]

[1] Research Institute of Physics, Southern Federal University, 344090 Rostov-on-Don, Russia; sitalo@sfedu.ru (E.I.S.); lashilkina@sfedu.ru (L.A.S.); lareznichenko@sfedu.ru (L.A.R.); glazunova@sfedu.ru (E.V.G.)
[2] Southern Scientific Center, Russian Academy of Science, 344006 Rostov-on-Don, Russia; nazarav@ssc-ras.ru
[3] School of Natural Sciences and Mathematics, Ural Federal University, 620000 Ekaterinburg, Russia; andrey.ushakov@urfu.ru (A.D.U.); vladimir.shur@urfu.ru (V.Y.S.)
* Correspondence: nboldyrev@sfedu.ru

Abstract: Ceramics of the quasi-binary concentration section ($0.1 \leq x \leq 0.2$, $\Delta x = 0.025$) of the ternary solid solution system (0.5 − x)$BiFeO_3$-0.5$PbFe_{0.5}Nb_{0.5}O_3$-$xPbTiO_3$ were prepared by the conventional solid-phase reaction method. An X-ray study at different temperatures revealed that (0.5 − x)BF-0.5PFN-xPT ceramics have a cluster morphology. Clusters have different modulation, crystal lattice symmetry, and chemical composition. The presence of a cluster structure in a solid solution with heterovalent substitution, consisting of regions rich in Ti^{+4}, Nb^{+5}, or Fe^{3+}, has led to the appearance of Maxwell–Wagner polarization in the studied ceramics. The study of the dielectric characteristics revealed the relaxor-like behavior of the studied ceramics. The grain morphology, dielectric, pyroelectric, and piezoelectric properties of the selected solid solutions were investigated. The highest piezoelectric coefficient, d_{33} = 280 pC/N, was obtained in the 0.3$BiFeO_3$-0.5$PbFe_{0.5}Nb_{0.5}O_3$-0.2$PbTiO_3$ ceramics. Study of the dielectric characteristics of all samples revealed relaxor ferroelectric behavior and a region of diffuse phase transition from the paraelectric to ferroelectric phase in the temperature range of 140–170 °C.

Keywords: dielectric properties; perovskites; multiferroics; piezoelectric properties; solid solutions

Citation: Boldyrev, N.A.; Sitalo, E.I.; Shilkina, L.A.; Nazarenko, A.V.; Ushakov, A.D.; Shur, V.Y.; Reznichenko, L.A.; Glazunova, E.V. Structure and Relaxor Behavior of (0.5 − x)$BiFeO_3$-0.5$PbFe_{0.5}Nb_{0.5}O_3$-$xPbTiO_3$ Ternary Ceramics. *Ceramics* **2023**, *6*, 1735–1748. https://doi.org/10.3390/ceramics6030106

Academic Editor: Dawei Wang

Received: 20 June 2023
Revised: 19 July 2023
Accepted: 31 July 2023
Published: 8 August 2023

1. Introduction

In recent years, multiferroic materials have attracted considerable attention in the scientific community due to the coexistence of ferroelectric, ferromagnetic, and ferroelastic ordering in those materials [1,2]. The multiple types of couplings present in these materials make them excellent candidates for a wide range of applications. Multiferroics can be used in alternating and permanent magnetic field sensors [3,4], memory elements [5,6], spintronic devices [7,8], artificial neural networks [9,10], and in other fields of modern engineering. $BiFeO_3$ (BF), which shows the rhombohedral perovskite structure (*R3c*) at room temperature, belongs to this class of multiferroic materials owing to the coexistence of ferroelectric (FE) and antiferromagnetic (AFM) orderings. The high ferroelectric Curie temperature (T_C~860 °C) and high antiferromagnetic Neel temperature (T_N~370 °C) make BF exhibit multiferroic properties at room temperature (RT); therefore, BF stands out from other single-phase multiferroic materials [11–14]. However, because of numerous disadvantages, such as a very high coercive field, high conductivity, low piezoelectric properties, and so on, the applications of BF single-phase material are still facing many large difficulties [15,16]. Lead iron niobate $PbFe_{0.5}Nb_{0.5}O_3$ (PFN) is another well-known multiferroic with a perovskite-type structure having the general chemical formula $A\left(B'_{0.5}B''_{0.5}\right)O_3$ and the diffuse phase transition from the paraelectric (PE) to the FE phase at T_C~114 °C. FE and AFM ordering coexist in it only below T_N~−140 °C [17]. Like BF, PFN is characterized

by increased electrical conductivity caused by the presence of ions of variable valence (Fe^{2+}/Fe^{3+}) and oxygen vacancies in their structure. Nevertheless, modification [18,19] or the creation of solid solutions [20,21] based on BF or PFN make it possible to stabilize the structure and improve the characteristics of the obtained ceramics. In order to enhance electric resistivity and multiferroic behavior, other ABO_3 perovskite compounds, such as $PbTiO_3$, $BaTiO_3$, $SrTiO_3$, and $PrFeO_3$, were combined with BF to form solid solutions with spontaneous magnetization [22–26]. In this sense, $PbTiO_3$ (PT), a well-known piezoelectric compound that has a tetragonal distorted perovskite structure (*P4mm* space group) and a ferroelectric phase transition at T_C ~490 °C, presents the necessary properties to enhance the properties of BF [27,28]. Desirably, binary BF-PT ceramics are synthesized very easily and display ferroelectric and antiferromagnetic properties at the same time. The BF-PT system displays a high ferroelectric transition temperature (T_C~367 °C) in the morphotropic phase boundary (MPB) region and maintains weak antiferromagnetic ordering at high temperatures (T_N~104 °C) [29], giving the BF-PT system considerable potential for applications in high-temperature fields. However, there are still some shortfalls for BF-PT, such as an extremely high coercive field (>150 kV/cm) and a low piezoelectric coefficient of d_{33}~50 pC/N, much lower than other piezoelectric ceramics [30–32]. In this regard, in recent years, considerable attention has been paid to obtaining new multiferroic materials by creating solid solutions of ternary systems based on multiferroics [33–37]. One of the promising systems is the (1-*x*-*y*)BF-*x*PFN-yPT ternary system, in which, according to the literature data [38,39] and our preliminary studies [40], there is MPB with coexisting rhombohedral (Rh) and tetragonal (T) phases. As is known, materials with MPB can demonstrate extreme properties and improve the electrophysical characteristics of the studied ceramic. In this regard, it is important to establish the regularities of the formation of structural, microstructural, dielectric, and piezoelectric characteristics of samples of the ternary system (1-*x*-*y*)BF-*x*PFN-*y*PT in the region of the phase diagram with a high PFN content. In this present work, we attempted to generalize the previous results of the study of this ternary system and refine the crystal structure features that strongly affect the ceramic macro responses.

2. Materials and Methods

Ceramic samples of the ternary system $(0.5 - x)$BF-0.5PFN-xPT ($0.1 \leq x \leq 0.2$, Δx = 0.025) were fabricated using conventional ceramic technology by double solid-phase synthesis at temperatures T_1 = 900 °C and T_2 = 950 °C and holding times $\tau_1 = \tau_2$ = 10 h, followed by sintering at T_{sin} = 1000 °C for 2 h. The initial reagents were Bi_2O_3, Fe_2O_3, PbO, TiO_2, and Nb_2O_5, with the content of the main substance not less than 99.95%. Samples for sintering were pressed into disks with a diameter of 10 mm and a thickness of 1 mm. After polishing, the electrodes were deposited onto the flat surfaces of the disks by stepwise firing of the silver paste at 200 °C for 20 min, 500 °C for 30 min, and 800 °C for 20 min.

X-ray studies in the temperature range $20 \leq T \leq 300$ °C were carried out using a diffractometer ADP-1 (Bragg–Brentano focusing) with $Co_{K\alpha}$ radiation. The temperature rise rate was arbitrary, the accuracy of temperature stabilization in the chamber was ±2 °C, and the isothermal exposure was 10 min. Changes in the structural parameters and phase state of the ceramics were monitored by the diffraction peaks $(111)_c$, $(200)_c$, and $(220)_c$. The diffraction peak profile was approximated by the Lorentz function. The error in measuring the parameters *a*, *b*, and *c* of the unit cell is $\Delta a = \Delta b = \Delta c = \pm(0.002–0.004)$ Å, the modulation wavelength, λ, was calculated by the formula (1):

$$\lambda = \left| \frac{1}{d_{hkl}} - \frac{1}{d_c} \right|^{-1}, \quad (1)$$

where d_{hkl} and d_c are the interplanar distances of the main peak and satellite, respectively [41].

The study of the ceramic grain structure was carried out using the KEYENCE VK-9700 color laser scanning 3D microscope.

Temperature dependences of the complex dielectric permittivity $\varepsilon^* = \varepsilon' - i\varepsilon''$ (ε' and ε'' are the real and imaginary parts of ε^*, respectively) were measured at 25–475 °C in the frequency range 10 Hz–100 kHz using a computer-controlled broadband dielectric spectrometer Novocontrol Concept 40 during continuous cooling or heating of the sample at a rate of 2–3 °C/min. Samples were polarized at T = 125 °C in the polyethylene siloxane fluid under applied fields of 3–6 kV/mm. Piezoelectric coefficients of the samples were measured at f = 110 Hz using a quasistatic YE2730A d33 METER (APC International Ltd., Mackeyville, PA, USA). Dielectric hysteresis loops were obtained at room temperature using a Sawyer–Tower circuit and oscilloscope. This allowed us to evaluate the residual polarization P_R and coercive field E_C of the samples.

The pyroelectric effect was measured by the dynamic method as described elsewhere [42]. Pyroelectric coefficient γ was determined by a dynamic technique using sinusoidal temperature modulation at a frequency of 2–3 Hz. The pyroelectric response was quantified by comparing it with a reference sample of the multicomponent PZT-based ceramic PCR-11 with a known value of the pyroelectric coefficient. All measurements were performed in the field-cooling and field-heating modes at a rate of 2–3 °C/min.

For the measurements of the small electric-field induced displacements and piezocoefficients, we used a single-beam Michelson–Morley laser interferometer modified with the lock-in amplifier and a PID feedback system described in [43,44]. External voltage was applied with an Agilent 33210A (Keysight Technologies, Santa Rosa, CA, USA) signal generator.

3. Results

3.1. XRD Analysis

The results of an X-ray diffraction study of 0.3BF-0.5PFN-0.2PT ceramics in the temperature range of 20–180 °C were presented in [45]. Therefore, in this paper, in the analysis of the crystal structure, we will focus on samples with $0.1 \leq x \leq 0.175$. It was shown in [46] that the average structure of ceramics with $0.1 \leq x \leq 0.15$ is cubic (C). However, the broadening of the diffraction peaks in the X-ray diffraction patterns indicates the presence of clusters with a symmetry other than C in the studied ceramic structure. The concentration phase transition from the C to the T phase in the range $0.175 \leq x \leq 0.2$ suggests that the clusters have a tetragonally distorted crystal lattice.

Figure 1 shows X-ray diffraction patterns of the solid solutions $(0.5 - x)$BF-0.5PFN-xPT ($0.1 \leq x \leq 0.175$) at the RT and diffraction peaks (200) and (220) at the different temperatures. Diffuse scattering near diffraction peaks at some temperatures transforms into satellite maxima, indicating the appearance of structure modulation. This is most noticeable in solid solutions with x = 0.15 and x = 0.175. The features of X-ray diffraction patterns include δ-like peaks, which, along with satellites, appear near diffraction reflections (dots on Figure 1). The explanation for the observed effects was given in [47], where numerical methods were used to study the intensity distribution of X-rays for a crystal consisting of randomly located domains with displacement waves λ_1 and λ_2 propagating along one of the crystallographic directions. It was shown by the authors of [47] that when the initial phases of displacement waves in neighboring domains are matched by the phase of the defect density wave (matching wave), δ-like peaks appear in the position corresponding to the wave vector of the defect density wave. In this case, periodically repeating crystallographic shear planes (CSPs) can be the cause of the defect density wave. CSPs are always present in a perovskite-type structure containing variable valence ions in B-positions (oxygen octahedra) [48–51]. In this case, the modulation wavelength calculated from the position of the δ-like peak with respect to diffraction reflection is the distance between CSPs, which, as shown in [52], are domain walls in ferroelectrics. The method from [47] makes it possible to characterize the real structure of solid solutions. Since the role of randomly located domains in ceramics can be played by clusters that differ in chemical composition, crystal lattice symmetry, modulation pattern, and other properties. The propagation of two modulation waves along one of the crystallographic directions in a

polycrystalline object can occur simultaneously in several crystallites. Therefore, two or more δ-like peaks can be expected in the X-ray diffraction pattern. Thus, a series of intense δ-like peaks are present on the satellites of the 220 reflections on the X-ray diffraction pattern of the ceramics with x = 0.175 (Figure 1d) at 80 °C. In the solid solutions with x = 0.1 and 0.125, the appearance of δ-like peaks is observed mainly near the 220 diffraction reflection (modulation in the <110> directions), while in the solid solutions with x = 0.15 and 0.175, they also appear near the 200 reflection (modulation in directions <100>). Peaks appear near the reflection 220 in the temperature range 30–300 °C, near the reflection 200—in the intervals 30–160 °C (x = 0.15) and 30–150 °C (x = 0.175). Near the 200 peaks at higher temperatures, δ-satellites do not appear, but the modulation of the structure is retained. Additional peaks corresponding to the difference or total wave vectors are not observed, which corresponds to a structure with non-interacting, randomly located domains [47].

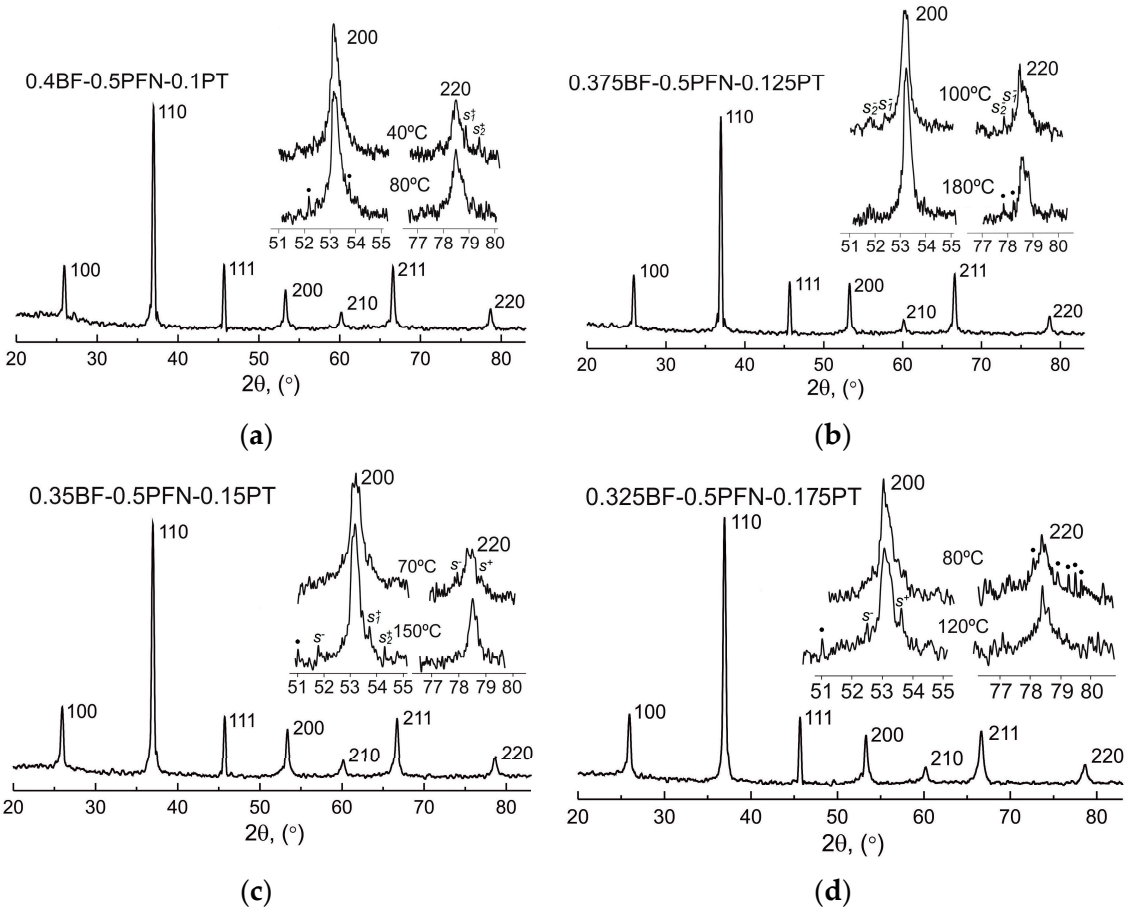

Figure 1. X-ray diffraction patterns of the studied ceramics at RT. (**a**–**d**) Diffraction peaks (200) and (220) with satellites at the different temperatures are shown in the insets.

The asymmetric position of the satellites relative to the diffraction reflection is another feature of the diffraction patterns. This may be caused by the fact that the structure of solid solutions includes regions whose crystal lattice consists of blocks of oxygen octahedra $m \times n$ (m, n is the number of octahedra) formed by two sets of almost orthogonal crystallographic shifts [48]. One of the structure-forming oxides of the studied solid solutions, Nb_2O_5, has a similar crystal lattice (block). If $m \neq n$, then each of the CSP sets creates its own displacement wave, which should lead to an asymmetric position of the satellites relative to the diffraction reflection.

Table 1 shows the modulation wavelengths in the directions <100> and <110> at the different temperatures. Wavelengths were calculated from satellites located on the smaller angle θ side (s^-) and on the bigger angle θ side (s^+) relative to diffraction reflection. It was

shown that the studied ceramics have a crystal lattice with sinusoidal modulation related to the concentration wave. Even-order satellites $\lambda_2 = \frac{1}{2}\lambda_1$ confirm the presence of the modulation (x = 0.125 at 100 °C, x = 0.15 at 150 °C). Asymmetric satellites are also observed on X-ray patterns of solid solutions with x = 0.15 at 70 °C and 190 °C and with x = 0.175 at 120 °C and 190 °C. Two wavelengths λ = 82(83) Å and λ = 77(78) Å are repeated in all solid solutions and probably correspond to the size of the domain, which is a block of oxygen octahedral 20.5 × 19.

Table 1. Modulation wavelengths, λ, in the directions <100> and <110>.

x	T, °C	λ, Å <100>		λ, Å <110>	
		c^-	c^+	c^-	c^+
0.1	40				$\lambda_1^+ = 331$ $\lambda_2^+ = 147$
	80	$\lambda^- = 109$		$\lambda_1^- = 117$ $\lambda_2^- = 77$	$\lambda^+ = 94$
0.125	100	$\lambda_1^- \approx 163$ $\lambda_2^- = 82$		$\lambda_1^- = 413$ $\lambda_2^- = 206$	
	110	$\lambda_1^- = 120$ $\lambda_2^- = 82$		$\lambda_1^- = 265$ $\lambda_2^- = 160$	
	180	$\lambda^- = 78$		$\lambda_1^- = 380$ $\lambda_2^- = 178$	
0.15	70			$\lambda^- = 240$	$\lambda^+ = 331$
	150	$\lambda^- = 83$	$\lambda_1^+ = 212$ $\lambda_2^+ = 105.5$		
	190	$\lambda^- = 82$	$\lambda^+ = 77$		
0.175	120	$\lambda^- = 190$	$\lambda^+ = 212$		
	190			$\lambda^- = 334$	$\lambda^+ = 201$
	240			$\lambda_1^- = 372$ $\lambda_2^- = 129$ $\lambda_3^- = 83$ δ-peak on satellite three $\lambda_\delta = 77$	

Thus, we assume that even-order satellites indicate sinusoidal (concentration) modulation, the asymmetric position of the satellites is associated with two-wave modulation in one of the <100> and <110> crystallographic directions, and the presence of δ-like peaks indicates the matching of the initial phases of the displacement waves by the matching wave. There are no satellites on the X-ray patterns corresponding to the sum and difference wave vectors. This is typical for a cluster structure with randomly located nanodomains that do not interact with each other. In each of the clusters of this structure, the electrical properties change in accordance with their chemical composition, which directly affects the smearing of the phase transition.

Figure 2 shows the temperature dependences of the width of the 200 and 111 peaks at half maximum (FWHM) and the unit cell parameter of the solid solution $(0.5 - x)$BF-0.5PFN-xPT. The existence of regions rich in titanium or niobium in the sample will lead to the fact that the dependences $a(T)$ in the <100> and <110> directions of the crystal lattice will differ. Therefore, the cell parameter was calculated from the (200) and (220)

diffraction peaks. The cell parameter constancy may be a sign of structural transformation (restructuring) in the corresponding temperature interval [53]. The change of the diffraction peaks at 111 and 200 FWHM makes it possible to suggest the symmetry of the region where the phase transition occurs. Thus, upon T → C transition, the FWHM of peak 200 decreases since the multiplet 002, 200 becomes a single peak, while the FWHM of peak 111 does not change. Upon Rh → C transition, the FWHM of peaks at 111 decreases (the multiplet 111, $11\bar{1}$ becomes a single peak), while the FWHM of peak 200 remains unchanged. During the monoclinic-cubic transition, the FWHM of both peaks decreases since both multiplets become single peaks. Table 2 shows the temperature ranges of the cell parameter constancy and the anomalous behavior of the $FWHM_{111}(T)$ and $FWHM_{200}(T)$ dependences.

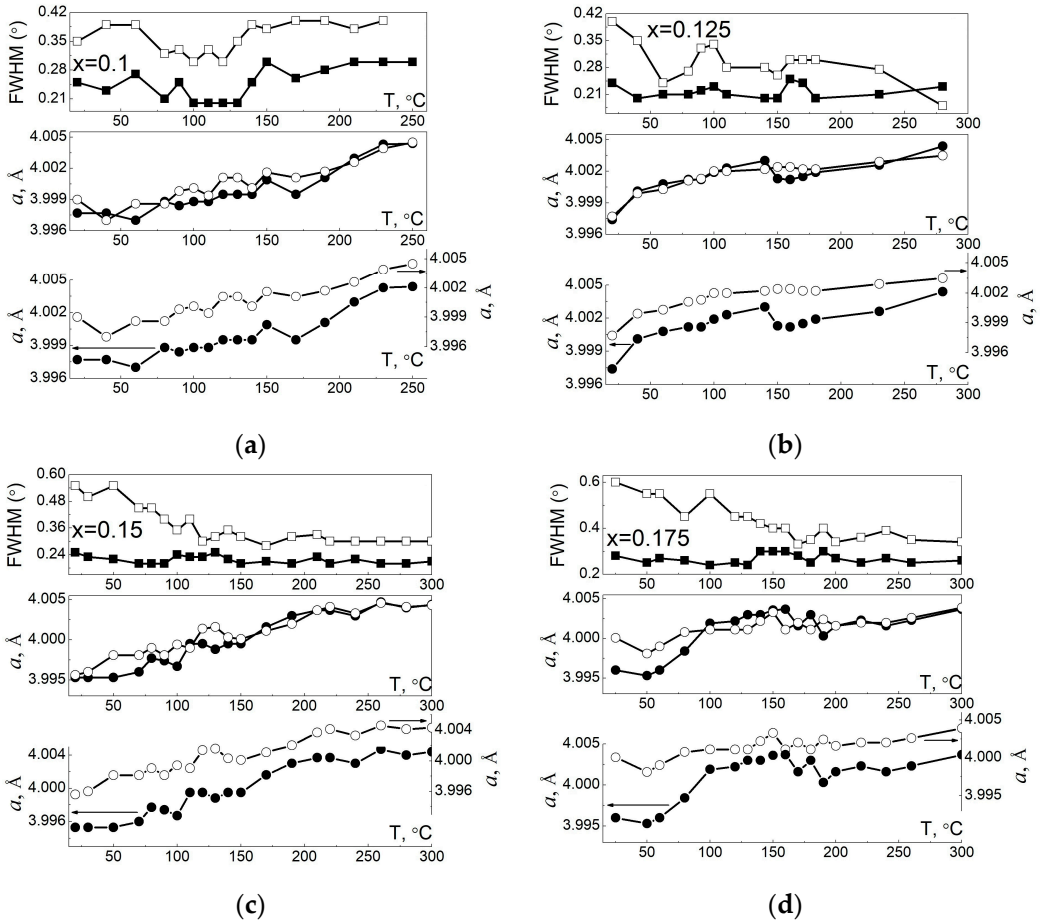

Figure 2. (**a**–**d**) Temperature dependences of the FWHM of peaks 200 (white squares) and 111 (black squares) and the cell parameter *a* (central and bottom panels) calculated from diffraction peaks 200 (black dots) and 220 (white dots). On the bottom panel, the cell parameter scale is deliberately enlarged and spaced apart in order to see the details of parameter changes in the <100> and <110> directions.

The dependences of the peaks 200 and 111 FWHM(T) in the sample with x = 0.1 (Figure 2a) have wide minimums in the intervals 80–120 °C and 100–130 °C, respectively, that indicate the presence of the monoclinic phase at 80–130 °C. The first interval includes the temperatures of two ferroelectric transitions in PFN at 80 °C and 120 °C. The wide temperature range of the transition in the ternary system is possibly related to the spread of the polarization rotation angle, similar to how it occurs in the single crystal of the binary system $0.67Pb(Mg_{1/3}Nb_{2/3})O_3$-$0.33PbTiO_3$ [54], where the monoclinic phase with different polarization rotation angles was found in the morphotropic region of the phase diagram. In [54], the authors explained the spread of polarization rotation angles (5°–35°) by the macro segregation and structure fluctuation generated in the process of cooling crystals to room temperature in the Bridgman method. However, the reason for the increase in FWHM

of both peaks above the phase transition temperature is not yet clear. Dependence $a_{200}(T)$ is a series of constancy segments rising stepwise from room temperature to 140 °C and at 230–250 °C, $a_{220} \approx const$ at 60–80 °C and at 120–130 °C. A wider range of cell parameter constancy (60–140 °C) as compared to the temperature range of the minimum half-widths of the 200 and 111 peaks (80–130 °C) can be associated with the presence of clusters with both T and R symmetry in the ceramics with x = 0.1.

Table 2. Temperature regions, ΔT °C, of the FWHM anomalous behavior and cell parameter constancy of the solid solutions $(0.5 - x)BiFeO_3$-0.5Pb$(Fe_{0.5}Nb_{0.5})O_3$-xPbTiO$_3$.

x	ΔT FWHM		ΔT a = const	
	200	**111**	**200**	**220**
0.1	80–120 (wide low)	100–130 (wide low)	20–40	60–80
			80–140	
			230–250	120–130
0.125	80–110 (max)	80–110 (halo)	80–90	100–180
	160–170 (halo)	160–170 (max)	150–160	
0.15	20–120 (decrease)	100–140 (halo)	110–150	60–110
			210–220	140–150
			260–300	260–300
0.175	20–170 (decrease)	140–170 (halo)	130–140	80–130
			150–160	160–180

In the sample with x = 0.125 (Figure 2b), both dependences FWHM(T) have two maxima at the same temperatures of 100 °C and 160 °C (Table 2). An increase in the half-width of the 111 and 200 diffraction peaks in the ranges of 80–110 °C and 160–170 °C can be caused, firstly, by the transition through an intermediate monoclinic phase [55] with multiplet peaks 111 and 200, and, secondly, by the decrease of the coherent scattering regions at the morphotropic transition or miniaturization of the average domain structure [56]. As a result, this leads to a broadening of the diffraction peaks.

In the sample with x = 0.15 and 0.175 FWHM of peak 200, the temperature decreases to 120 °C and 170 °C, respectively, due to a decrease in the degree of cell distortion in clusters with tetragonal symmetry. The halo of the FWHM 111 peak is observed in the intervals of 100–140 °C (x = 0.15) and 130–170 °C (x = 0.175). Its appearance is most likely associated with the T → K transition in clusters through an intermediate monoclinic phase and/or with the miniaturization of the average domain structure [56]. The dependence $a(T)$ in ceramics with x = 0.175, calculated from two diffraction lines, differs only at low temperatures, with a_{200} sharply increasing in the range of 50–100 °C while a_{220} increasing gradually. This may be due to the fact that the Ti-rich regions with tetragonal distortion have a more mobile structure than the Nb-rich regions. As mentioned above, the structure of the latter consists of blocks formed by two sets of almost orthogonal crystallographic shifts and, therefore, is not as mobile as in titanium-rich regions. A wide range of temperature anomalies is most likely caused by different concentrations of lead and titanium in the clusters. This concentration determines the c/a value and the FE → PE transition temperature. Table 2 shows that the intervals $a = const$ for a_{200} and a_{220} overlap and coincide with the temperatures of the FWHM anomalies. Consequently, phase transitions with a change in symmetry in clusters occur in the structure of ceramics with x = 0.15 and 0.175, just as in the samples described above.

Thus, close X-ray analysis showed that $(0.5 - x)$BF-0.5PFN-xPT ceramics have a cluster morphology. Clusters differ in modulation character, crystal lattice symmetry, chemical composition, and, consequently, electrical characteristics and FE → PE transition

temperatures. Such morphology with heterovalent substitution, consisting of regions rich in Ti^{+4}, Nb^{+5}, or Fe^{3+}, can lead to the appearance of Maxwell–Wagner polarization at the grain boundaries.

3.2. Microstructural Characterization

Figure 3 shows photographs of the microstructure of the studied ceramics. The grain structure of sample $x = 0.1$ is inhomogeneous and consists of large crystallites in the form of irregular polyhedra. The split occurs both along the grain boundary and along the grains themselves, which indicates approximately equal strength of grains and grain boundaries (or intergranular interlayers). The crystallite size varies from ~15 μm to ~25 μm. With an increase in the PT concentration, the average grain size sharply decreases to 10 μm (Figure 3b). The cracking passes through the intergranular spaces. It indicates that the grains have become stronger than the boundaries. In addition, traces of fluxes and intergranular interlayers can be observed in the sample with $x = 0.125$, indicating a change in the sintering method—from solid-phase to sintering with the participation of a liquid phase (LP). Low-melting Bi-containing compounds of eutectic origin formed during the synthesis can be the main components of this LP. Another possible source of the appearance of the LP is the relatively low-melting lead oxide with a melting point of 838 °C (in the composition 0.5 PbO–0.5 TiO_2 [57]). This is confirmed by the fact that with a further increase in the PT concentration, the number of fluids increases. A further increase in the concentration of PT ($0.15 \leq x \leq 0.2$) leads to a decrease in the size of grains of all types, an increase in the number of fluxes, and some strengthening of ceramics (Figure 3c–e). Grain refinement can also be associated with an increased heterogeneity of the crystal structure, which stimulates recrystallization processes with the simultaneous formation of many centers of primary recrystallization with a reduced mass capacity. Grain and strength characteristics have been discussed in more detail in [45].

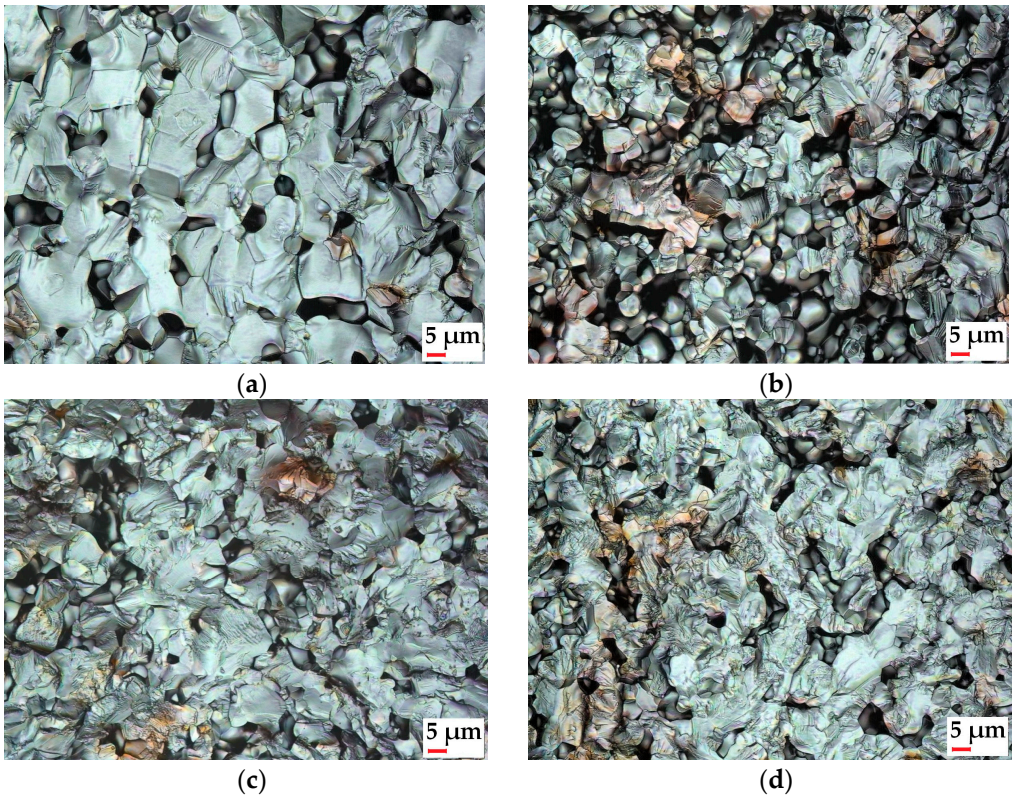

Figure 3. *Cont.*

(**e**)

Figure 3. Microstructure of the studied ceramics (**a**) $x = 0.1$, (**b**) $x = 0.125$, (**c**) $x = 0.15$, (**d**) $x = 0.175$, and (**e**) $x = 0.2$.

3.3. Dielectric and Piezoelectric Characteristics

There are two maxima on the dependencies of $\varepsilon'/\varepsilon_0(T)$ in the temperature ranges 130–170 °C and 250–400 °C. In all samples, the temperature of both maxima (T_{m1} and T_{m2}) shifts to higher temperatures as f increases, which is typical for relaxor ferroelectrics. The degree of smearing and the values of permittivity at the maximum point of the second one are much higher than those of the first one. The second maximum is most likely associated with the effects of Maxwell–Wagner polarization and relaxation of charge carriers at grain boundaries. Additionally, the first one (Figure 4a) corresponds to the phase transition from the ferroelectric to the paraelectric phase, which occurs in clusters of the T phase (in objects with $0.1 \leq x \leq 0.15$) and in the MPB ($x = 0.175$, 0.2). On the whole, the studied samples demonstrate the behavior of relaxor ferroelectrics with a phase transition in the region of 140–170 °C. The dielectric loss tangent (tanδ) at temperatures above 240 °C begins to rise sharply due to the increase in conductivity (Figure 4b).

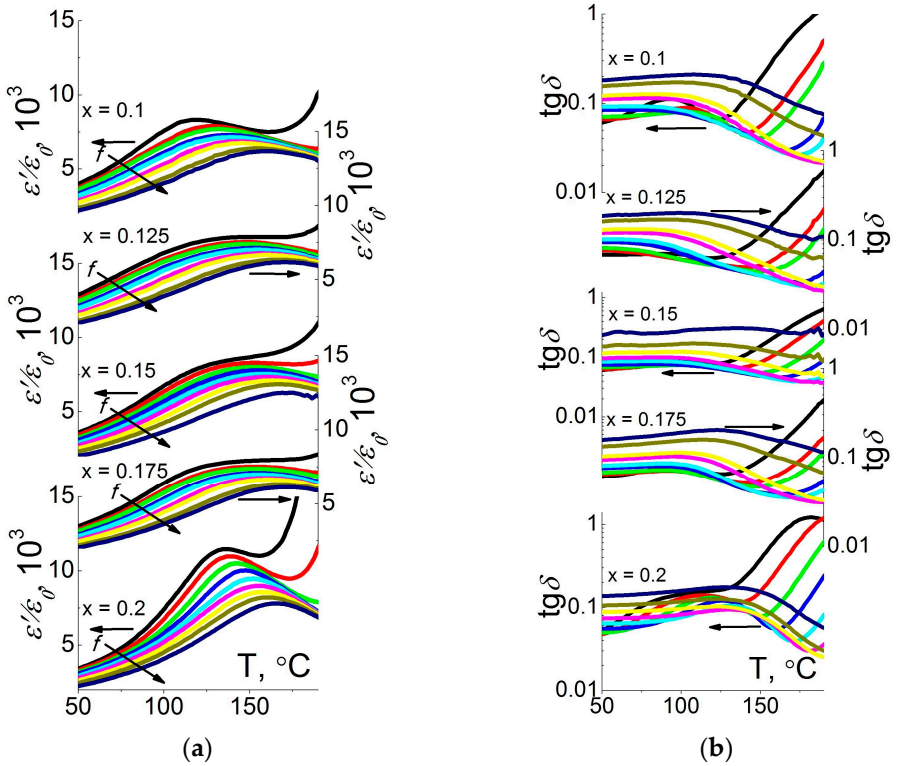

Figure 4. (**a**,**b**) Temperature dependences of dielectric constant and dielectric loss tangent in the temperature range (50–190 °C) and frequency range (50–10^6 Hz). The dependences are arranged from top to bottom as the concentration of PT increases.

It was possible to observe the piezoelectric characteristics that were stable over time in several samples of the studied ceramics. The value of d_{33} increases with increasing PT concentration. The highest piezoelectric constant is ~280 pC/N for 0.3BF-0.5PFN-0.2PT ceramic. The remanent polarization and coercive field in this sample are ~12 μC/cm^2 and ~9 kV/cm, respectively. Compared to the (1-*x*)BF-*x*PT system, the E_C of 0.3BF–0.5PFN-0.2PT ceramics is reduced to make the samples easier to be poled [58].

4. Discussion

When approximating the $T_{m1}(f)$ dependence in the whole frequency range, we used the Vogel–Fulcher relation (2) (Figure 5):

$$f = f_0 e^{\frac{E_a}{k(T_{m1}-T_f)}}, \quad (2)$$

where f_0 is the frequency of attempts to overcome a potential barrier E_a, k is the Boltzmann constant, and T_f is the Vogel–Fulcher temperature, interpreted as the temperature of "static freezing" of electric dipoles or transition to the state of a dipole glass.

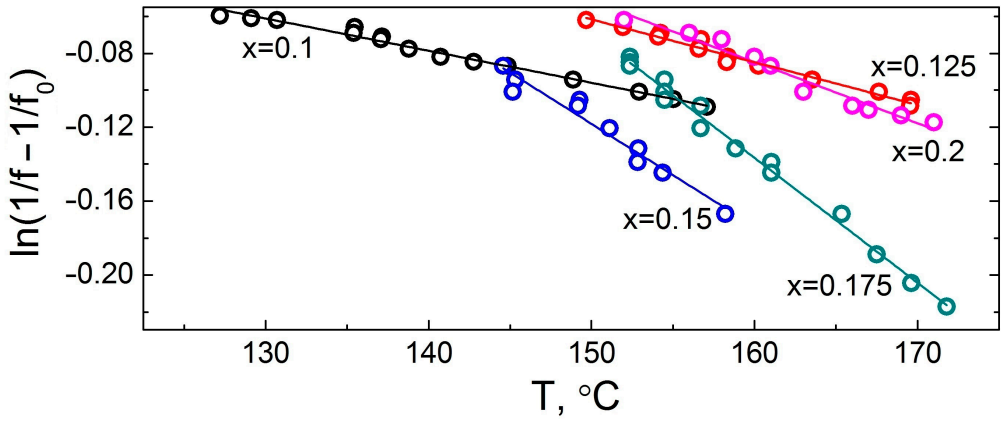

Figure 5. Dependences $\ln(1/f - 1/f_0)(T)$ for the studied ceramics.

The calculated values of E_{act} and T_f for all samples lie in the ranges (0.15–0.45) eV and (100–120) °C, respectively. The obtained results indicate that the studied samples are relaxor ferroelectrics. The smearing of the phase transition in the studied ceramics can be associated with the presence of non-interacting clusters with different modulation, crystal lattice symmetry, and chemical composition identified by X-ray analysis.

The calculated values of the Burns temperature (T_b) determined from the $(\varepsilon'/\varepsilon_0)^{-1}(T)$ dependences, corresponding to the temperature of the polar nanoregions, exceeded the T_{m1} values by more than 100 °C. This indicates that the FE phase clusters in the studied ceramics disappear only at T > 240 °C.

The fact that the first maximum in the dependences $\varepsilon'/\varepsilon_0(T)$ corresponds to a phase transition is also confirmed by measurements of the piezoelectric modulus in the low fields and the pyroelectric coefficient γ (Figure 6). As an example, Figure 6 shows the temperature dependences of these parameters for the 0.325BF-0.5PFN-0.175PT ceramics. At a temperature of 145–150 °C, the pyrosignal disappears, i.e., the polarization of the sample vanishes, which most likely corresponds to the Curie temperature in this composition. The figure clearly shows the maximum temperature dependence of the low-field piezoelectric coefficient d_{33} for all compositions, which is shifted towards low temperatures from the T_C. The presence of this maximum and its value indicate the "predisposition" of each sample to the polarization process in order to obtain the maximum piezoelectric coefficient d_{33}.

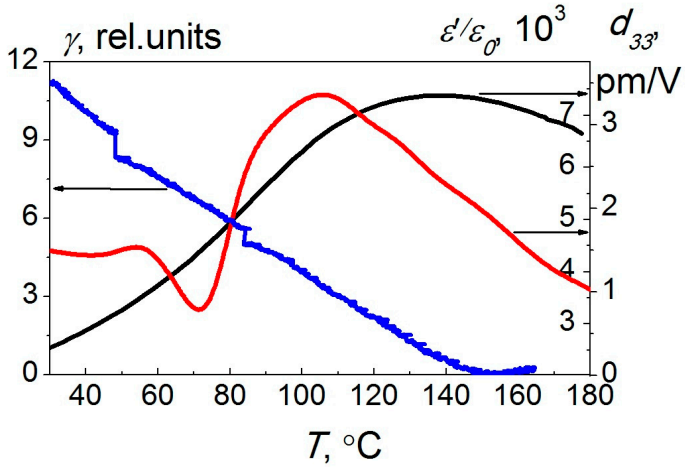

Figure 6. Temperature dependences of the dielectric constant (black) at 1 kHz, pyroelectric coefficient γ (blue), and weak field piezoelectric modulus (red) of the 0.325BF-0.5PFN-0.175PT ceramics.

5. Conclusions

Ceramic samples of solid solutions of the ternary system $(0.5 - x)BiFeO_3$-$xPbFe_{0.5}Nb_{0.5}O_3$-$xPbTiO_3$ ($0.1 \leq x \leq 0.2$, $\Delta x = 0.025$) were prepared by the conventional solid-phase reaction method. Using X-ray studies, it was found that at $0.10 \leq x \leq 0.15$, the objects have a cubic crystal structure containing segregations (clusters) with tetragonal symmetry of the crystal lattice, and at $x = 0.175$, 0.20, a morphotropic phase boundary with coexisting T and C phases is formed. An X-ray study at different temperatures revealed that $(0.5 - x)$BF-0.5PFN-xPT ceramics have a cluster morphology. These non-interacting clusters have different modulation, crystal lattice symmetry, and chemical composition. However, to unambiguously confirm the presence of clusters, it is necessary to use additional methods, such as SFM and TEM, which will be undertaken in future work. We assume that the presence of a cluster structure in a solid solution with heterovalent substitution, consisting of regions rich in Ti^{+4}, Nb^{+5}, or Fe^{3+}, has led to the appearance of Maxwell–Wagner polarization in the studied ceramics. The study of the dielectric characteristics revealed the relaxor-like behavior of the studied ceramics. A diffuse phase transition, which corresponds to the first maximum on the $\varepsilon'/\varepsilon_0(T)$ dependences, occurs in the range 140–170 °C in the clusters of the T phase ($0.10 \leq x \leq 0.15$) and in the tetragonal part of the MPB ($x = 0.175$, 0.20). The phase transition at these temperatures is confirmed by X-ray studies as well as by measurements of the pyroelectric coefficients γ and the piezoelectric modulus in weak fields. The second maximum on the $\varepsilon'/\varepsilon_0(T)$ dependences is associated with the effects of Maxwell–Wagner polarization and relaxation of charge carriers at the grain boundaries. In the samples from MPB, it was possible to observe high and stable piezoelectric responses. The maximum values of the piezoelectric modulus were observed in the 0.3BF-0.5PFN-0.2PT ceramics (~280 pC/N). The results show that 0.325BF-0.5PFN-0.175PT and 0.3BF-0.5PFN-0.2PT ceramics are promising materials for future investigation in consideration of their dielectric and piezoelectric properties.

Author Contributions: Conceptualization, N.A.B. and E.I.S.; X-ray analysis, L.A.S.; microstructural analysis, A.V.N.; resources, E.V.G.; piezoelectric properties investigation, A.D.U. and V.Y.S.; writing—original draft preparation, N.A.B.; writing—review and editing, E.I.S.; visualization, N.A.B.; supervision, L.A.R. and L.A.S.; project administration, L.A.R.; funding acquisition, L.A.R. All authors have read and agreed to the published version of the manuscript.

Funding: This research was funded by the Ministry of Science and Higher Education of the Russian Federation (a state task in the field of scientific activity in 2023). Project No. FENW-2023-0010/(GZ0110/23-11-IF).

Data Availability Statement: The data presented in this study are available on request from the corresponding author.

Acknowledgments: Work was performed using the equipment of the Center for Collective Use "Electromagnetic, Electromechanical and Thermal Properties of Solids", Research Institute of Physics, Southern Federal University, and the Center for Collective Use of the Southern Scientific Center of the Russian Academy of Science (Rostov-on-Don, Russia). The equipment of the Ural Center for Shared Use "Modern nanotechnology" Ural Federal University (Reg. No. 2968).

Conflicts of Interest: The authors declare no conflict of interest.

References

1. Saije, K.H. *Phase Transformations in Ferroelastic and Co-Elastic Solids*; Cambridge University Press: Cambridge, UK, 1990.
2. Pyatakov, A.P.; Zvezdin, A.K. Magnetoelectric and multiferroic media. *Phys. Uspekhi* **2012**, *55*, 557–581. [CrossRef]
3. Zhai, J.; Xing, Z.; Dong, S.; Li, J.; Viehland, D. Detection of pico-Tesla magnetic fields using magneto-electric sensors at room temperature. *Appl. Phys. Lett.* **2006**, *88*, 062510. [CrossRef]
4. Gao, J.; Jiang, Z.; Zhang, S.; Mao, Z.; Shen, Y.; Chu, Z. Review of Magnetoelectric Sensors. *Actuators* **2021**, *10*, 109. [CrossRef]
5. Tehrani, S.; Slaughter, J.M.; Deherrera, M.; Engel, B.N.; Rizzo, N.D.; John Salter, J.; Durlam, M.; Dave, R.W.; Janesky, J.; Butcher, B.; et al. Magnetoresistive random access memory using magnetic tunnel junctions. *Proc. IEEE* **2003**, *91*, 703. [CrossRef]
6. Bibes, M.; Barthélémy, A. Towards a magnetoelectric memory. *Nat. Mater.* **2008**, *7*, 425–426. [CrossRef] [PubMed]
7. Chang, S.-J.; Chung, M.-H.; Kao, M.-Y.; Lee, S.-F.; Yu, Y.-H.; Kaun, C.-C.; Nakamura, T.; Sasabe, N.; Chu, S.-J.; Tseng, Y.-C. $GdFe_{0.8}Ni_{0.2}O_3$: A multiferroic material for low-power spintronic devices with high storage capacity. *ACS Appl. Mater. Interfaces* **2019**, *11*, 31562–31572. [CrossRef]
8. Gajek, M.; Béa, H.; Bibes, M.; Bouzehouane, K. Spintronics with multiferroics. In Proceedings of the IEEE International Magnetics Conference (INTERMAG), San Diego, CA, USA, 8–12 May 2006.
9. Borders, W.A.; Akima, H.; Fukami, S.; Moriya, S.; Kurihara, S.; Horio, Y.; Sato, S.; Ohno, H. Analogue spin-orbit torque device for artificial-neural-network-based associative memory operation. *Appl. Phys. Express* **2008**, *10*, 013007. [CrossRef]
10. Lu, P.-P.; Shen, J.-X.; Shang, D.-S.; Sun, Y. Artificial synaptic device based on a multiferroic heterostructure. *J. Phys. D Appl. Phys.* **2019**, *52*, 465303. [CrossRef]
11. Venevtsev, Y.N.; Zhdanov, G.; Solov'ev, S. The internal fields in ferroelectric crystal of $PbTiO_3$. *Sov. Phys. Crystallogr.* **1960**, *6*, 218–224.
12. Smolenskii, G.A.; Isupov, V.; Agranovskaya, A.; Krainik, N.N. New ferroelectrics of complex composition. *Sov. Phys. Solid State* **1961**, *2*, 2651–2654.
13. Chen, J.C.; Wu, J.M. Dielectric properties and ac conductivies of dense single-phased $BiFeO_3$ ceramics, Appl. *Phys. Lett.* **2007**, *91*, 182903.
14. Ramachandran, B.; Rao, M.S. Low temperature magnetocaloric effect in polycrystalline $BiFeO_3$ ceramics. *Appl. Phys. Lett.* **2009**, *95*, 142505. [CrossRef]
15. Fischer, P.; Polomska, M.; Sosnowska, I.; Szymanski, M. Temperature dependence of the crystal and magnetic structures of $BiFeO_3$. *J. Phys. C Solid State Phys.* **1980**, *13*, 1931. [CrossRef]
16. Kiselev, S.V.; Ozerov, R.P.; Zhdanov, G.S. Detection of magnetic order in ferroelectric $BiFeO_3$ by neutron diffraction. *Sov. Phys. Dokl.* **1963**, *7*, 742.
17. Venevtsev, Y.N.; Gagulin, V.V.; Lyubimov, V.N. *Ferroelectromagnets*; Nauka: Moscow, Russia, 1982.
18. Khasbulatov, S.V.; Pavelko, A.A.; Shilkina, L.A.; Reznichenko, L.A.; Gadjiev, G.G.; Bakmaev, A.G.; Magomedov, M.-R.M.; Omarov, Z.M.; Aleshin, V.A. Phase composition, microstructure, and thermophysical and dielectric properties of multiferroic $Bi_{1-x}Dy_xFeO_3$. *Thermophys. Aeromech.* **2016**, *23*, 445–450. [CrossRef]
19. Pavlenko, A.V.; Boldyrev, N.A.; Reznichenko, L.A.; Verbenko, I.A.; Konstantinov, G.M.; Shilkina, L.A. Microstructure and dielectric and piezoelectric properties of $PbFe_{0.5}Nb_{0.5}O_3$ ceramics modified with Li_2CO_3 and MnO_2. *Inorg. Mater.* **2014**, *50*, 750–756. [CrossRef]
20. Boldyrev, N.A.; Pavlenko, A.V.; Shilkina, L.A.; Reznichenko, L.A.; Miller, A.I. Structure and dielectric characteristics of (1–x)$BiFeO_3$–x$PbTiO_3$ solid solutions. *Bull. Russ. Acad. Sci. Phys.* **2016**, *80*, 733–735. [CrossRef]
21. Laguta, V.V.; Stephanovich, V.A.; Raevski, I.P.; Raevskaya, S.I.; Titov, V.V.; Smotrakov, V.G.; Eremkin, V.V. Magnetoelectric effect in antiferromagnetic multiferroic $Pb(Fe_{1/2}Nb_{1/2})O_3$ and its solid solutions with $PbTiO_3$. *Phys. Rev. B* **2017**, *95*, 014207. [CrossRef]
22. Kumar, M.M.; Srinivas, A.; Suryanarayana, S.V. Structure property relations in $BiFeO_3$/$BaTiO_3$ solid solutions. *J. Appl. Phys.* **2000**, *87*, 855–862. [CrossRef]
23. Ivanova, T.L.; Gagulin, V.V. Dielectric properties in the microwave range of solid solutions in the $BiFeO_3$-$SrTiO_3$ system. *Ferroelectrics* **2002**, *265*, 241–246. [CrossRef]
24. Sai Sunder, V.V.S.S.; Halliyal, A.; Umarji, A.M. Investigation of tetragonal distortion in the $PbTiO_3$–$BiFeO_3$ system by high-temperature x-ray diffraction. *J. Mater. Res.* **1995**, *10*, 1301–1306. [CrossRef]
25. Mahesh Kumar, M.; Srinivas, A.; Suryanarayana, S.V.; Kumar, G.S.; Bhimasankaram, T. An experimental setup for dynamic measurement of magnetoelectric effect. *Bull. Mater. Sci.* **1998**, *21*, 251–255. [CrossRef]
26. Balamurugan, K.; Harish Kumar, N.; Santhosh, P.N. Multiferroic properties of $Bi_{1/2}Sr_{1/2}FeO_3$. *J Appl Phys.* **2009**, *105*, 07D909. [CrossRef]

27. Lee, S.W.; Shim, K.B.; Auh, K.H.; Knott, P. Ferroelectric anomaly in the differential thermal analysis of $PbTiO_3$ glass. *Mater. Lett.* **1999**, *38*, 356–359. [CrossRef]
28. Burnett, T.L.; Comyn, T.P.; Merson, E.; Bell, A.J.; Mingard, K.; Hegarty, T.; Cain, M. Electron backscatter diffraction as a domain analysis technique in $BiFeO_3$-$PbTiO_3$ single crystals. *IEEE Trans. Ultrason. Ferroelectr. Freq. Control* **2008**, *55*, 957–962. [CrossRef]
29. Comyn, T.P.; McBride, S.P.; Bell, A.J. Processing and electrical properties of $BiFeO_3$–$PbTiO_3$ ceramics. *Mater. Lett.* **2004**, *58*, 3844–3846. [CrossRef]
30. Cheng, J.; Meng, Z. Piezoelectric performances of lead-reduced $(1-x)(Bi_{0.9}La_{0.1})(Ga_{0.05}Fe_{0.95})O_3$-$x(Pb_{0.9}Ba_{0.1})TiO_3$ crystalline solutions in the morphotropic phase boundary. *J. Appl. Phys.* **2004**, *96*, 6611–6615. [CrossRef]
31. Zhang, S.; Xia, R.; Randall, C.A.; Shrout, T.R.; Duan, R. Dielectric and piezoelectric properties of niobium-modified $BiInO_3$–$PbTiO_3$ perovskite ceramics with high Curie temperatures. *J. Mater. Res.* **2005**, *20*, 2067–2071. [CrossRef]
32. Sehirlioglu, A.; Sayir, A.; Dynys, F. High temperature properties of $BiScO_3$–$PbTiO_3$ piezoelectric ceramics. *J. Appl. Phys.* **2009**, *106*, 014102. [CrossRef]
33. Zhuang, J.; Zhao, J.; Su, L.-W.; Wu, H.; Bokov, A.A.; Ren, W.; Ye, Z.-G. Structure and local polar domains of Dy-modified $BiFeO_3$-$PbTiO_3$ multiferroic solid solutions. *J. Mater. Chem. C* **2015**, *3*, 12450–12456. [CrossRef]
34. Lin, Q.; He, C.; Long, X. Structural, electric and magnetic properties of $BiFeO_3$-$Pb(Mg_{1/3}Nb_{2/3})O_3$-$PbTiO_3$ ternary ceramics. *J. Electroceram.* **2016**, *36*, 8–15. [CrossRef]
35. Ahlawat, A.; Satapathy, S.; Choudhary, R.J.; Singh, M.K.; Gupta, P.K. Observation of magnetoelectric coupling in $BiFeO_3$-($Pb(Mg_{1/3}Nb_{2/3})O_3$-$PbTiO_3$) composites. *Mater. Lett.* **2016**, *181*, 123–126. [CrossRef]
36. Abhilash, J.J.; Goel, S.; Hussain, A.; Kumar, B. Ferro-/pyroelectric response of 0.57BF-0.31PMN-0.12PT ternary ceramic faraway from morphotropic phase boundaries. *Ceram. Int.* **2017**, *43*, 16676–16683.
37. Hu, W.; Tan, X.; Rajan, K. Piezoelectric Ceramics with Compositions at the Morphotropic Phase Boundary in the $BiFeO_3$–$PbZrO_3$–$PbTiO_3$ Ternary System. *J. Am. Ceram. Soc.* **2011**, *94*, 4358–4363. [CrossRef]
38. Pang, D.; He, C.; Han, S.; Pan, S.; Long, X.; Tailor, H. A new multiferroic ternary solid solution system of $BiFeO_3$–$Pb(Fe_{1/2}Nb_{1/2})O_3$–$PbTiO_3$. *J. Eur. Ceram. Soc.* **2015**, *35*, 2033–2040. [CrossRef]
39. Pang, D.; He, C.; Long, X. Ferroelectric and antiferromagnetic properties of a ternary multiferroic $BiFeO_3$-$Pb(Fe_{1/2}Nb_{1/2})O_3$-$PbTiO_3$ single crystal. *Ceram. Int.* **2016**, *42*, 19433–19436. [CrossRef]
40. Boldyrev, N.A.; Pavlenko, A.V.; Shilkina, L.A.; Nazarenko, A.V.; Bokov, A.A.; Reznichenko, L.A.; Rudskaya, A.G.; Panchenko, E.I. Structure, microstructure, dielectric and piezoelectric properties of (1-x-y)$BiFeO_3$-x$PbFe_{0.5}Nb_{0.5}O_3$-yPbTiO3 ceramics. *Ceram. Int.* **2019**, *45*, 14768–14774. [CrossRef]
41. Guinier, A. *X-ray Diffraction of Crystals*; Publishing House of Physics and Mathematics Literature: Moscow, Russia, 1961.
42. Raevskaya, S.I.; Zakharov, Y.u.N.; Lutokhin, A.G.; Emelyanov, A.S.; Raevski, I.P.; Panchelyuga, M.S.; Titov, V.V.; Prosandeev, S.A. Critical nature of the giant field-induced pyroelectric response in $Pb(Mg_{1/3}Nb_{2/3})O_3$–x$PbTiO_3$ single crystals. *Appl. Phys. Lett.* **2008**, *93*, 042903. [CrossRef]
43. Ushakov, A.D.; Mishuk, E.; Makagon, E.; Alikin, D.O.; Esin, A.A.; Baturin, I.S.; Tselev, A.; Shur, V.Y.; Lubomirsky, I.; Kholkin, A.L. Electromechanical properties of electrostrictive CeO_2:Gd membranes: Effects of frequency and temperature. *Appl. Phys. Lett.* **2017**, *110*, 142902. [CrossRef]
44. Ushakov, A.D.; Yavo, N.; Mishuk, E.; Lubomirsky, I.; Shur VYa Kholkin, A.L. Electromechanical Measurements of Gd-Doped Ceria Thin Films by Laser Interferometry. In Proceedings of the ASRTU Conference Proceedings, IV Sino-Russian ASRTU Symposium on Advanced Materials and Processing Technology, Ekaterinburg, Russia, 23–26 June 2016.
45. Sitalo, E.I.; Boldyrev, N.A.; Shilkina, L.A.; Nazarenko, A.V.; Nagaenko, A.V.; Reznichenko, L.A. Structure, microstructure, dielectric and piezoelectric properties of (1-x-y)$BiFeO_3$-x$PbFe_{0.5}Nb_{0.5}O_3$-y$PbTiO_3$ ceramics. *J. Adv. Dielectr.* **2022**, *12*, 2160023. [CrossRef]
46. Boldyrev, N.A.; Sitalo, E.I.; Shilkina, L.A.; Nazarenko, A.V.; Lutokhin, A.G.; Reznichenko, L.A. Structure and high piezoelectric response of the ternary 0.3$BiFeO_3$-0.5$PbFe_{0.5}Nb_{0.5}O_3$-0.2$PbTiO_3$ ceramics. *Ferroelectrics* **2022**, *590*, 99–109. [CrossRef]
47. Ustinov, A.I.; Olikhovskaya, L.A.; Shmyt'ko, I.M. X-ray diffraction in polydomain crystals modulated by transverse waves of atomic displacements. 2. Two-wave modulation of crystals. *Crystallogr. Rep.* **2000**, *45*, 374–379. [CrossRef]
48. Rao, C.N.R.; Gopalakrishnan, J. *New Directions in Solid State Chemistry*; Cambridge University Press: Cambridge, UK, 1986.
49. Tret'yakov, Y.D. *Chemistry of Nonstoichiometric Oxides*; Moscow State University Press: Moscow, Russia, 1974.
50. Reznichenko, L.A.; Shilkina, L.A.; Titov, S.V.; Razumovskaya, O.N.; Titov, V.V.; Shevtsov, S.I. Defect structure of alkaline-earth, cadmium, and lead titanates. *Inorg. Mater.* **2005**, *41*, 492–502. [CrossRef]
51. Reznichenko, L.A.; Shilkina, L.A.; Gagarina, E.S.; Yuzyuk, Y.u.I.; Razumovskaya, O.N.; Kozinkin, A.V. Crystallographic Shear in Niobium Oxides of Different Compositions. *Crystallogr. Rep.* **2004**, *49*, 820–827. [CrossRef]
52. Al Meitzler, H. Structural transformations occasioned by crystallographic shear in PLZT and TiO_2 ceramics. *Ferroelectrics* **1975**, *11*, 503–510. [CrossRef]
53. Reznichenko, L.A.; Shilkina, L.A.; Razumovskaya, O.N.; Kravchenko, O.Y.; Akhnazarova, V.V. The Invar Effect and the Devil's Staircase in Alkali and Alkaline Earth Niobates. *Crystallogr. Rep.* **2006**, *51*, 87–95. [CrossRef]
54. Xu, G.; Luo, H.; Xu, H.; Yin, Z. Third ferroelectric phase in PMNT single crystals near the morphotropic phase boundary composition. *Phys. Rev. B* **2001**, *64*, 020102(R). [CrossRef]

55. Noheda, B. Structure and high-piezoelectricity in lead oxide solid solutions. *Curr. Opin. Solid State Mater. Sci.* **2002**, *6*, 27–34. [CrossRef]
56. Schönau, K.A.; Schmitt, L.A.; Knapp, M.; Fuess, H.; Eichel, R.-A.; Kungl, H.; Hoffmann, M.J. Nanodomain structure of $PbZr_{1-x}Ti_xO_3$ at its morphotropic phase boundary: Investigations from local to average structure. *Phys. Rev. B* **2007**, *75*, 184117. [CrossRef]
57. Jaffe, B.; Cook, W.R., Jr.; Jaffe, H. *Piezoelectric Ceramics*; Academic Press: New York, NY, USA, 1971.
58. Comyn, T.P.; Stevenson, T.; Bell, A.J. Piezoelectric properties of $BiFeO_3$—$PbTiO_3$ ceramics. *J. Phys. IV* **2005**, *128*, 13–17.